

Attosecond photoelectron microscopy of H_2^+

S. X. Hu*

Laboratory for Laser Energetics, University of Rochester, 250 E. River Road, Rochester, New York 14623, USA

L. A. Collins

Theoretical Division, Los Alamos National Laboratory, Los Alamos, New Mexico 87545, USA

B. I. Schneider

Office of Cyberinfrastructure and Physics Division, National Science Foundation, Arlington, Virginia 22230, USA

(Received 13 May 2009; published 31 August 2009)

We present a numerical study of the ultrafast ionization dynamics of H_2^+ exposed to attosecond extreme ultraviolet (xuv) pulses that goes beyond the Born-Oppenheimer approximation. The four-dimensional, time-dependent Schrödinger equation was solved using a generalization of the finite-element discrete-variable-representation/real-space-product technique used in our previous calculations to include the dynamical motion of the nuclei. This has enabled us to expose the target to any polarized light at arbitrary angles with respect to the molecular axis. Calculations have been performed at different angles and photon energies ($\hbar\omega=50$ eV up to 630 eV) to investigate the energy and orientation dependence of the photoionization probability. A strong orientation dependence of the photoionization probability of H_2^+ was found at a photon energy of $\hbar\omega=50$ eV. At this energy, we found that the ionization probability is three times larger in the perpendicular polarization than in the parallel case. These observations are explained by the different geometric “cross sections” seen by the photoejected electron as it leaves the molecule. This ionization anisotropy vanishes at the higher-photon energy of $\hbar\omega\geq 170$ eV. When these higher-energy xuv pulses are polarized perpendicular to the internuclear axis, a “double-slit-like” interference pattern is observed. However, we find that the diffraction angle only approaches the classical formula $\phi_n=\sin^{-1}(n\lambda_e/R_0)$, where n is the diffraction order, λ_e is the released electron wavelength, and R_0 is the internuclear distance, when $n\lambda_e$ becomes less than 65% of R_0 . These results illustrate the possibility of employing attosecond pulses to perform photoelectron microscopy of molecules.

DOI: [10.1103/PhysRevA.80.023426](https://doi.org/10.1103/PhysRevA.80.023426)

PACS number(s): 33.80.Rv, 32.80.Rm

I. INTRODUCTION

Attosecond xuv pulses generated in atomic gases or on surfaces by high harmonics have attracted considerable attention in atomic, molecular, and optical (AMO) physics in recent years [1–3] and currently form a very active branch of high-field physics [4]. They enable researchers to observe, in real time, numerous ultrafast processes in nature, including pumping atoms and molecules to initiate Auger decay [5] and atomic electron tunneling [6], as well as probing these systems to explore intra-atomic electron correlations [7], electron tunneling between molecular centers [8], and mapping of molecular wave packets [9]. Furthermore, attosecond xuv pulses can be used to steer electron-wave packets [10] and to enhance high-order harmonic radiation [11]. To gain better control of imaging these ultrafast processes with intense attosecond xuv pulses requires a quantitative understanding of the dynamical response of atomic and molecular targets to such nonperturbative electromagnetic field interactions.

Full-dimensional quantum calculations have been conducted for one-, two-, and many-electron atoms exposed to intense optical and/or xuv pulses [12–15]. In contrast to the atomic cases, full-dimensional molecular responses to such

nonperturbative pulses that describe all electronic and nuclear degrees of freedom on an equal footing have not as yet been performed, even for the simplest molecular system H_2^+ . Treatments to date have been divided into two groups [7,16–19]: First, application of the Born-Oppenheimer (BO) approximation, in which the nuclear and electronic motions decouple, allowed us to calculate full electron wave functions at a series of fixed-nuclear positions. Averaging over the nuclear wave functions produced the characteristics of vibration and dissociation. Second, restricting the dimensionality of the electronic motion made possible full coupling to the nuclear movement. In addition, classical Monte Carlo approaches [20], in which all degrees of freedom are treated fully dynamically, do exist. Prior to this study, the most sophisticated quantum calculations that involved nuclear vibration used a three-dimensional (3D) model [21–23] for intense field-molecule interactions, which describes the two-dimensional (2D) electronic motion in the cylindrical coordinates (ρ, z) (assuming axial symmetry) and the one-dimensional (1D) nuclear motion along molecular axis R . This model can only represent linearly polarized pulses parallel to the molecular axis because axial symmetry is assumed. In addition to the direct discretization of the multidimensional wave function on a grid, there have been other methods that use single-center expansions in a spherical-harmonic basis [24]. However, to obtain fully converged results, such methods require a very large number of spherical harmonics, especially for circularly polarized radiation.

*shu@lle.rochester.edu

In this paper, we proceed a step further by accounting for the full 3D electronic and 1D nuclear motion in intense field-molecule interactions. Nuclear rotation is ignored for being far too slow with respect to the pulse lengths considered. Thus, we are left with a four-dimensional (4D) problem (x, y, z, R) . This 4D treatment enables us to consider any polarization at any angle (θ) with respect to the molecular axis. These large-scale, 4D calculations become practical only after applying the finite-element discrete variable representation (FEDVR) to the four coordinates. The FEDVR method [25,26] has previously been applied to a number of atomic and molecular problems with great success. This technique makes possible a flexible distribution on the grid that maintains high accuracy and keeps the number of basis functions small.

A variety of strong-field problems exist that are well suited to our 4D code, including H_2^+ dissociation and ionization in circularly polarized intense laser pulses. The example presented here focuses on the ultrafast dynamics of H_2^+ exposed to intense attosecond xuv pulses at different photon energies and polarization orientations. We found that the attosecond photoionization probability of H_2^+ is dependent on orientation at a photon energy of $\hbar\omega=50$ eV, while such behavior disappears at high-photon energies ($\hbar\omega \geq 170$ eV). On the other hand, high-energy photoionization exhibits a “double-slit-like” interference pattern when the xuv pulse is polarized perpendicular to the molecular axis. Many of these observations are directly connected to the de Broglie wavelength of the ejected electron. This particular application emphasizes the 3D character of the electron-field interaction and depends weakly on the nuclear motion. This example serves not only to explore interesting orientation effects for ultrashort pulses but also to benchmark the 4D formulation against our fixed-nuclei codes in a regime in which the BO approximation should basically hold. Our future studies will examine cases of more severe nonadiabaticity.

This paper is organized as follows: The basic formalism and numerical implementation are presented in Sec. II. Results and discussions appear in Sec. III. Section IV contains observations and concluding remarks. Atomic units $\hbar=m=e=1$ apply throughout this paper with lengths in bohr $a_{\text{bohr}}=5.291 \times 10^{-8}$ cm, energy in hartrees (27.21 eV), and time in units of 2.42×10^{-17} s.

II. FORMALISMS AND NUMERICAL PROCEDURES

The simplest hydrogen molecular ion (H_2^+ , HD^+ , D_2^+ , ...) forms a typical three-body system as shown by the schematic diagram in Fig. 1 with the motion of the two nuclei [with mass and charge (M_1, q_1) and (M_2, q_2)] characterized by their position vectors \mathbf{R}'_1 and \mathbf{R}'_2 and that of the electron (m, e) by its position vector \mathbf{r}' . Hiskes [27] has shown that by choosing the center of mass (\mathbf{O}) of the two nuclei as the origin the three-body motion separates into a center of mass (\mathbf{R}_C) and internal (\mathbf{R}, \mathbf{r}) components, with vectors \mathbf{R} and \mathbf{r} representing, respectively, the internuclear distance and the position of the electron with respect to the center of mass of the two nuclei. After several algebraic manipulations, the total kinetic energy operator can be expressed as

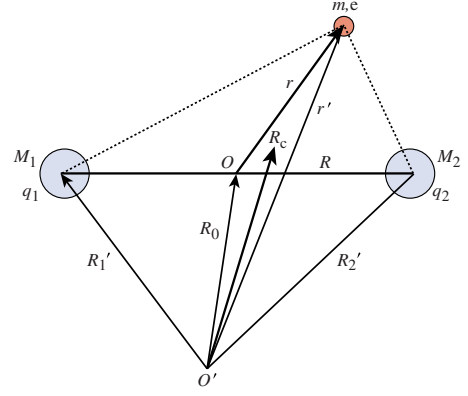


FIG. 1. (Color online) The schematic diagram of a hydrogen molecular ion H_2^+ .

$$K(\mathbf{R}_C, \mathbf{R}, \mathbf{r}) = -\frac{1}{2M} \frac{\partial^2}{\partial \mathbf{R}_C^2} - \frac{1}{2\mu_N} \frac{\partial^2}{\partial \mathbf{R}^2} - \frac{1}{2\mu_e} \frac{\partial^2}{\partial \mathbf{r}^2}, \quad (1)$$

with the reduced masses $\mu_N = M_1 M_2 / (M_1 + M_2)$, $\mu_e = m(M_1 + M_2) / M$ and the total mass $M = m + M_1 + M_2$. The first term describes the independent system center-of-mass motion.

The Coulomb interaction has the following form:

$$V_C(\mathbf{R}, \mathbf{r}) = \frac{q_1 q_2}{|\mathbf{R}|} - \frac{q_1 e}{|\mathbf{r} + \mu_2 \mathbf{R}|} - \frac{q_2 e}{|\mathbf{r} - \mu_1 \mathbf{R}|}, \quad (2)$$

where $\mu_1 = M_1 / (M_1 + M_2)$ and $\mu_2 = M_2 / (M_1 + M_2)$. Finally, invoking the dipole approximation, the time-dependent field-interaction terms become

$$V_I(\mathbf{R}, \mathbf{r}, t) = -\frac{M_1 - M_2}{M_1 + M_2} \mathbf{e} \mathbf{E}(t) \cdot \mathbf{R} + \left(1 + \frac{m}{m + M_1 + M_2}\right) \mathbf{e} \mathbf{E}(t) \cdot \mathbf{r} \quad (3)$$

in the length gauge. For a homonuclear species like H_2^+ and D_2^+ the first term in Eq. (3) vanishes. The electron-nuclei coupling mediates the energy transfer from the field to the nuclei. Since we neglect the system center-of-mass motion, we are left with the following time-dependent Schrödinger equation (TDSE) for the internal dynamics of an intense field-driven hydrogen molecular ion:

$$i \frac{\partial}{\partial t} \Psi(\mathbf{R}, \mathbf{r}; t) = [K + V_C + V_I] \Psi(\mathbf{R}, \mathbf{r}; t), \quad (4)$$

where K consists of only the second and third terms in Eq. (1). This equation constitutes a complete six-dimensional (6D) TDSE with the field-free molecular Hamiltonian given by $H_0 = K + V_C$.

The ability to align molecules with strong laser pulses has witnessed significant progress in recent years [28]. In addition, the cold-target recoil-ion-momentum spectroscopy (COLTRIMS) technique is capable of measuring complete molecular fragmentation at any fixed configuration relative to laser polarization [29]. Under these circumstances, the nuclear rotation effects can be neglected and the 6D TDSE

can be reduced to four dimensions, consisting of the full 3D electronic motion and the 1D nuclear vibration. In Cartesian coordinates the final 4D TDSE has the form

$$i\frac{\partial}{\partial t}\Psi(x,y,z,R;t)=[K+V_C+V_I]\Psi(x,y,z,R;t). \quad (5)$$

To solve the above Schrödinger equation [Eq. (5)], we employed the FEDVR method to span the 4D Cartesian coordinate space. Combining the FEDVR with the real-space-product algorithm [30], we have developed a parallelized multidimensional time propagator, whose implementation details appear elsewhere [26]. Representative examples of 3D applications to spatially extended systems include (1) attosecond pump-probe of He atoms [7], (2) circularly polarized strong-field interactions with molecules [7,16], (3) electron-Rydberg atom collisions and Coulombic three-body interactions [31], and (4) Bose-Einstein condensates [32]. With the FEDVR method, we distribute grid points naturally following the potential gradient. Along the laser polarization direction, we have generally used several hundred finite elements, with a four-point basis within each element. The size of each finite element increases outward from the vicinity of the nuclei. The smallest spatial grid is about ~ 0.07 bohr, which yields a total number of points of $\sim 3 \times 10^9$ and requires a time step of the order of $\sim 5 \times 10^{-3}$ a.u.,. Such large spatial grids guarantee that 99.9% of the wave packet resides within the computation box at the end of the calculation, although absorption boundaries are still employed to avoid unphysical reflections [33]. For parallelization, we have applied a 2D spatial decomposition within the MPI scheme. This 4D code displays nearly linear scaling up to ~ 1600 processors on supercomputers for such large-scale calculations. For attosecond photoionization of H_2^+ presented here, each calculation takes about 15 h using 480 processors on the Coyote supercomputer (AMD dual core processors) at Los Alamos National Laboratory.

III. RESULTS AND DISCUSSION

A. Ground state

As an initial condition, we choose the ground state of 4D H_2^+ determined using imaginary time (IT: $t \rightarrow i\tau$) propagation of Eq. (5). Under the transformation to imaginary time, an initial arbitrary wave packet will evolve into the unnormalized ground-state wave function for long propagation times. As shown in Figs. 2(a) and 2(b), the total system energy and the expectation value of the internuclear distance $\langle R \rangle$ approach $E_0 \approx -0.5872$ a.u. and $\langle R \rangle \approx 2.0248$ a.u., respectively. The errors are within $\leq 1.3\%$ of the analytical values of $E_{\text{tot}} = -0.59243$ a.u. and $\langle R \rangle = 2.0$ a.u. [34]. Finally, the ground-state probability density is plotted in the x - y plane and the x - R plane in Figs. 2(c) and 2(d) with the molecular axis along the x axis.

B. Photoionization anisotropy

We considered attosecond xuv pulses linearly polarized in the x , y plane, at any angle θ with respect to the molecular axis R (along the x axis). The case of $\theta=0^\circ$ ($\theta=90^\circ$) corre-

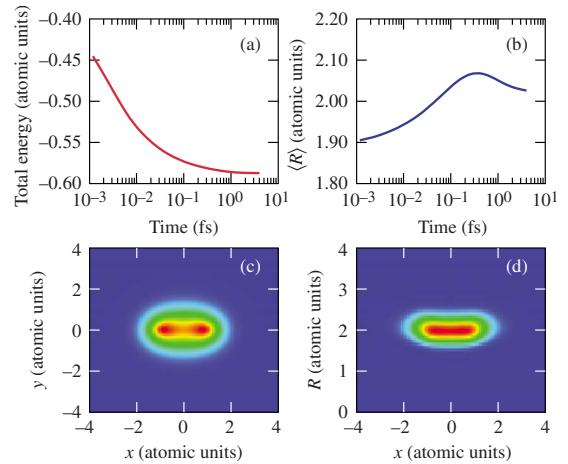


FIG. 2. (Color online) The ground state of 4D H_2^+ obtained from imaginary-time propagation: (a) the system energy as a function of propagation time, (b) the expectation value of internuclear distance $\langle R \rangle$ versus propagation time, (c) the probability density profile on the x - y plane, and (d) the probability density profile on the x - R plane.

sponds to the laser polarization parallel (perpendicular) to the molecular axis. In Figs. 3–7 we present results for a xuv photon energy of $\hbar\omega=50$ eV. As shown in Fig. 3, the xuv pulse has a \sin^2 envelope with a pulse duration of 500 attoseconds (asec) and a field strength of 0.53 a.u. (10^{16} W/cm 2).

With time-dependent calculations, we can trace the dynamics of the field-molecule interaction in great detail. For example, we can monitor the ground-state population change during the pulse interaction. The results appear in Fig. 4 for the three cases considered: parallel ($\theta=0^\circ$) (red dashed-dotted line), perpendicular ($\theta=90^\circ$) (blue dashed line), and “tilted” ($\theta=45^\circ$) (green solid line). We have used the same grid parameters for all three calculations. The ground-state populations adiabatically follow the field variation, but with a doubled frequency because both positive and negative oscillations of the field deplete the ground state in the same way. At the end of the xuv pulse, we observe three times more ground-state depletion from the perpendicular as com-

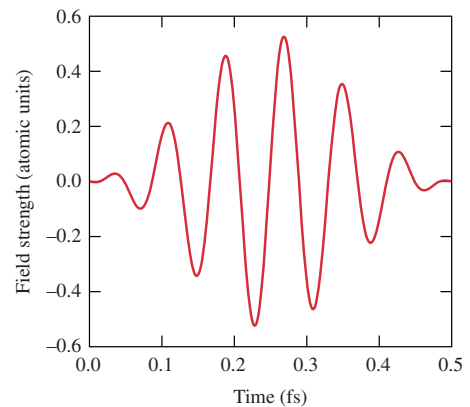


FIG. 3. (Color online) The concerned xuv pulse has a photon energy of $\hbar\omega=50$ eV, a peak field strength of $E_0 \approx 0.53$ a.u., and a pulse length of $\tau=500$ asec with a \sin^2 envelope.

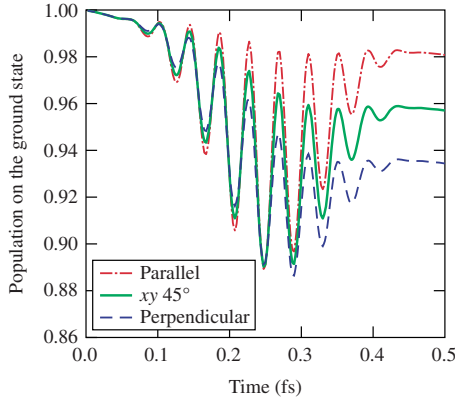


FIG. 4. (Color online) The time-dependent ground-state population of H_2^+ driven by attosecond xuv pulses ($\hbar\omega=50$ eV) polarized in parallel (red dashed-dotted line), in perpendicular (blue dashed line), and “tilted” $\theta=45^\circ$ relative to the molecular axis in the x , y plane (green solid line), respectively. A strong orientation dependence of the ground-state depletion is observed.

pared to the parallel orientation, with the tilted ($\theta=45^\circ$) case lying in between. An examination of the history of the population depletion shown in Fig. 4 indicates that the release of ground-state population occurs in a similar fashion for the three cases (similar population “dips”) but that the “rescattering” of the wave packets driven back over the molecular potential by the field behave in a dramatically different fashion. In the parallel case, the wave packets driven back by the field recombine mostly to the ground state, as indicated by the higher-population peaks. In contrast, the returning wave packets in the perpendicular configuration scatter mostly away from the ground state, as shown by the continuously dropping population peaks (blue dashed line).

To better understand such an orientation dependency, we calculated the total energy change ($\langle H_0 \rangle - E_0$) during the pulse interaction. Figure 5 shows the results for the three cases. The perpendicular orientation considerably facilitates an energy exchange between the field and the molecule,

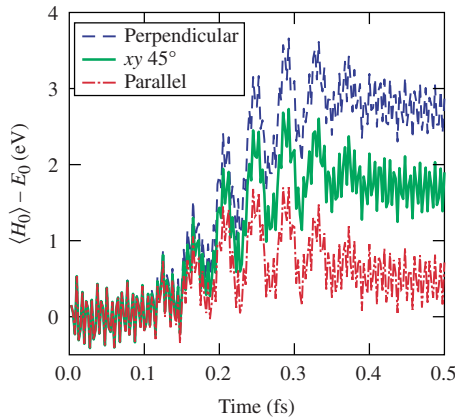


FIG. 5. (Color online) The molecular system’s energy change [$\langle H_0 \rangle - E_0$] during the attosecond pulse interaction ($\hbar\omega=50$ eV), for parallel polarization (red dashed-dotted line), perpendicular polarization (blue dashed line), and 45° -tilted polarization relative to the molecular axis in the x - y plane (green solid line), respectively.

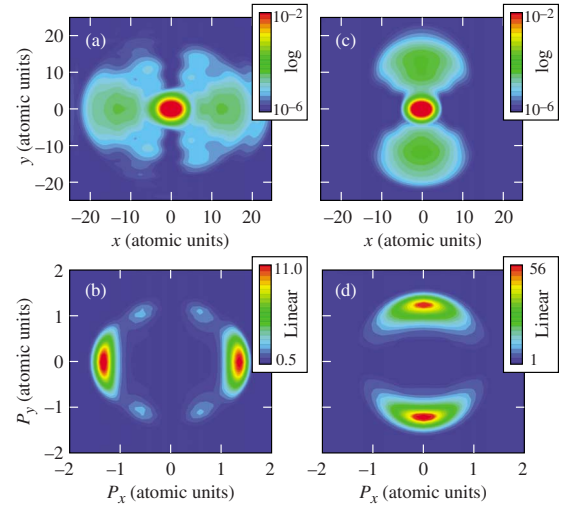


FIG. 6. (Color online) The electron probability densities of H_2^+ at the end of the attosecond xuv pulses ($\hbar\omega=50$ eV) for (a) parallel polarization and (c) perpendicular polarization. The corresponding momentum distributions of the ejected photoelectrons are shown in (b) and (d), respectively. The ionization probability is three times higher for the perpendicular polarization than that of the parallel polarization.

yielding more than three times energy absorption than the parallel ($\theta=0^\circ$) case. Greater energy absorption at $\theta=90^\circ$ implies a larger excitation/ionization probability, which is consistent with the larger ground-state depletion seen in Fig. 4.

Snapshots of the probability density in the x , y plane of configuration space are plotted in Figs. 6(a) and 6(c) at the end of xuv pulse for $\theta=0^\circ$ and 90° . The corresponding ionization momentum distributions are shown in Figs. 6(b) and 6(d), respectively. By integrating the electron probability in regions larger than ~ 5 a.u. away from the molecular center, we find, not unexpectedly, that the ionization probability becomes more than three times higher in the perpendicular than in the parallel case. This observed ionization difference between orientations appears independent of the xuv pulse intensity. Overall, the ejected electron momentum spectrum

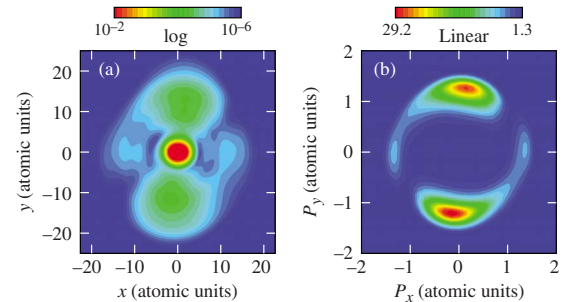


FIG. 7. (Color online) (a) The pulse-ending snapshot of electron probability density of H_2^+ for the case of tilted polarization ($\theta=45^\circ$) with respect to the molecular axis (x axis); (b) the corresponding photoelectron momentum distribution in the x - y plane. It is noted that the ejected photoelectron peaks off the polarization axis, which is a result of the orientation dependence of the attosecond photoionization of H_2^+ .

peaks at values that conserve the energy for single-photon absorption, i.e., $\hbar\omega - I_p = E_K \approx 20$ eV. Although electrons are ejected in line with the xuv pulse polarization for these two cases, slightly different features arise. For example, small-amplitude features appear at large angles in the parallel case [Figs. 6(a) and 6(b)], which may be associated with the field-driven wave packets from one center to scatter on the other. This feature is absent in the perpendicular case although the more extended distribution in the momentum spectrum may mask weak scattering signatures.

The orientation dependence of H_2^+ photoionization observed above has a consequence for a generally tilted pulse polarization in that the directions of the electron ejection and the xuv polarization can differ. To illustrate such a situation, we have plotted probability density snapshots in Fig. 7(a) for the case of $\theta=45^\circ$ as well as the corresponding ionization momentum spectrum [Fig. 7(b)]. Instead of aligning with the xuv polarization direction, the probability density for the ejected electron now peaks at $\theta \approx 82^\circ$. The linearly polarized field ($\theta=45^\circ$) can be equally decomposed to x and y components, for which the y -component field induces more ionization than the x component. Thus, the overall ionization wave packets tend to “bend” to the y axis. This ionization anisotropy found in the xuv regime appears opposite to that observed in a recent experiment on molecular tunneling ionization anisotropy in H_2 for intense optical fields [19,35], which found slightly more ($\sim 30\%$) ionization in the parallel orientation. We have performed temporal 4D calculations for HD^+ in the optical few-cycle regime, which behaves similar to the experimental trend [19,35]. In the optical regime, the ejected electron has a wide range of energy from a few eV to a few hundred eV due to the multiphoton/tunneling ionization by the intense field. Very low-energy electrons have de Broglie wavelengths much larger than the molecular size and show no directional preference. On the other hand, for high-energy electron ejections, the ionization along the parallel polarization direction slightly dominates. Therefore, the overall tunneling ionization, given by the sum over all electron spectra, shows a less dramatic anisotropy than for single-photon ionization in the xuv regime.

To gain further insights into the orientation dependence, we observe that for a photon energy of $\hbar\omega=50$ eV, the ejected electron ($E_K \approx 20$ eV) has a de Broglie wavelength of $\lambda_e \approx 5.2$ a.u., more than twice the internuclear distance. Therefore, for the perpendicular direction (y axis), an electron (wave packet) driven back by the field cannot distinguish between the two molecular “scattering” centers and, consequently, experiences a much larger combined geometrical cross section for rescattering, as compared to the case of parallel polarization. For the latter situation, the returning electron wave packets always encounter aligned single-center rescattering. We should therefore intuitively expect a more extended momentum distribution for perpendicular polarization. To characterize the extent of the momentum distribution, we take as a measure the angular spread Φ , estimated by the angle at which the probability drops to $1/e$ of its peak value. We find for perpendicular polarization that $\Phi \approx 35^\circ$, certainly exceeding the $\Phi \approx 24^\circ$ for parallel polarization [see Figs. 6(b) and 6(d)]. A large cross section for rescattering essentially facilitates the efficient photon absorp-

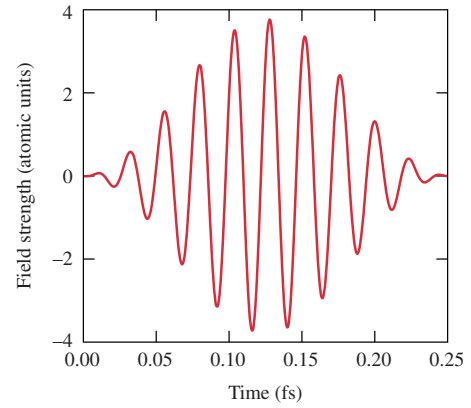


FIG. 8. (Color online) The xuv pulse with a photon energy of $\hbar\omega=170$ eV, a peak field strength of ~ 3.76 a.u., and a pulse length of $\tau=250$ asec.

tion, thereby resulting in more ionization. If the above explanation is correct, such an orientation dependence of molecular photoionization should disappear once the photoelectron de Broglie wavelength decreases (increasing $\hbar\omega$) since once the photoelectron can distinguish each scattering center, the rescattering takes a uniform distribution. To test this hypothesis, we have performed calculations at $\hbar\omega=170$ eV for both perpendicular and parallel polarizations. The 250-asec xuv pulse is plotted in Fig. 8. To have a noticeable ionization probability, we now increase the peak-field strength to 3.76 a.u. (5×10^{17} W/cm 2).

The results are shown in Figs. 9 and 10, respectively, for the ground-state depletion history and the total system energy change. From Fig. 9, we see that the final population left in the ground state is roughly similar for both situations, although the parallel polarization results in slightly higher ionization probability. A similar conclusion emerges from the field-molecule energy exchange as shown by Fig. 10.

Finally, we plot the probability density snapshots in Figs. 11(a) and 11(c) for the parallel and perpendicular polarization cases as well as the corresponding momentum distributions of ionized electron wave packets in Figs. 11(b) and

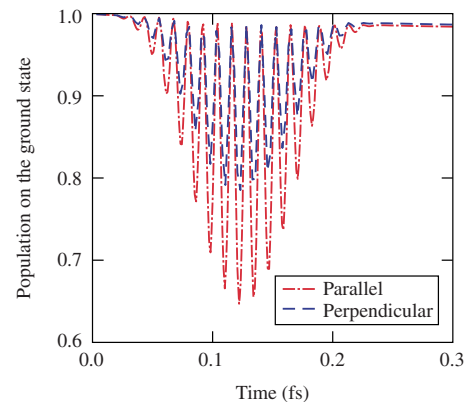


FIG. 9. (Color online) The time-dependent ground-state population of H_2^+ driven by high photon-energy attosecond xuv pulses ($\hbar\omega=170$ eV), whose polarizations are either parallel (red dashed-dotted line) or perpendicular (blue dashed line) to the molecular axis.

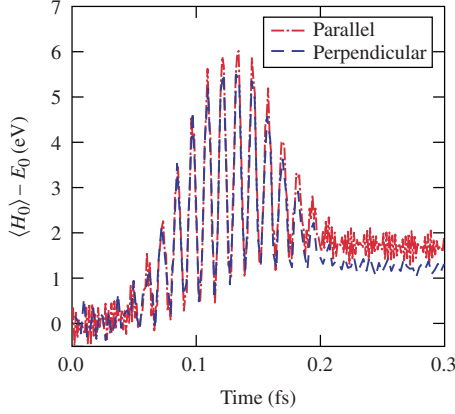


FIG. 10. (Color online) The molecular system’s energy change $[\langle H_0 \rangle - E_0]$ versus the interaction time ($\hbar\omega = 170$ eV), for both parallel polarization (red dashed-dotted line) and perpendicular polarization (blue dashed line).

11(d). We find that the ionization probability, obtained from integrating over regions of $r > 5$ a.u. from the molecular center, is roughly the same for these two cases. Namely, the dramatic orientation dependence of H_2^+ photoionization, observed at a low-photon energy of $\hbar\omega = 50$ eV, disappears at $\hbar\omega = 170$ eV. The total ionization probability can be inferred from one minus the final population (P_{GS}) left on the ground state. From Fig. 9 we observe the similar values of P_{GS} for both parallel and perpendicular cases. Thus, the ionization probability does not show the orientation dependence at higher-photon energies. Once again, this is because the released “fast” electron ($E_K \approx 140$ eV) now has a de Broglie wavelength of $\lambda_e \approx 1.96$ a.u., which is slightly smaller than the internuclear distance. Thus, the released electron can distinguish the two molecular scattering centers, with the consequences being that the ionization does not depend drastically on the rescattering direction.

C. Interference effects

We further examine the double-slit-like interference patterns that appear in perpendicular polarization [Figs. 11(b) and 11(d)]. All of the interference peaks reside within the momentum circle dictated by energy conservation ($E_K = \hbar\omega - I_p$). Basically, the photoelectron wave packets released from each center interfere, producing electrons ejected in specific directions. This behavior was discussed by Cohen and Fano almost a half a century ago [36] as well as recently by Walter and Briggs [37]. This phenomenon has also been modeled using time-independent methods within the Born-Oppenheimer approximation [38,39]. Their calculations were performed at a slightly larger photon energy ($\hbar\omega = 250$ eV) than the one shown in Fig. 11 and were compared with measurements using circularly polarized light [40]. For $\hbar\omega = 170$ eV, our time-dependent results show that the first interference peak appears at an angle of $\phi_1 \approx 52^\circ$ relative to the polarization y axis. Young’s double-slit formula, $R_0 \sin(\phi_n) = n\lambda_e$ used in time-independent studies [38], predicts the first peak at $\phi_1 \approx 75^\circ$ for the associated photon energy. Here, R_0 is the internuclear distance, λ_e is the de Bro-

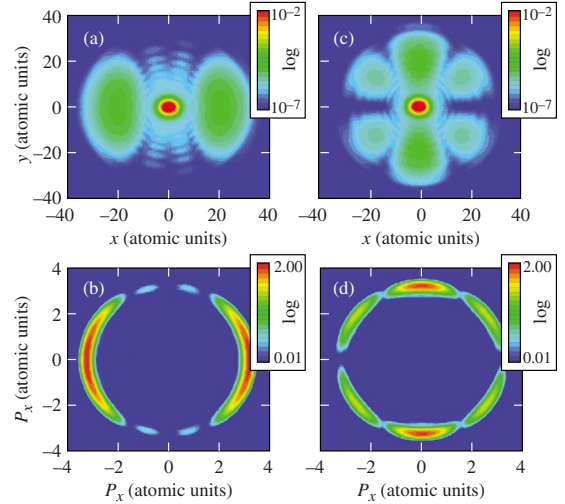


FIG. 11. (Color online) The electron probability densities of H_2^+ at the end of the attosecond xuv pulses ($\hbar\omega = 170$ eV) for (a) parallel polarization and (c) perpendicular polarization. The corresponding momentum distributions of the ejected photoelectrons are shown in (b) and (d), respectively. “Double-slit-like” interference patterns are observed for the perpendicular polarization case. The orientation dependence of attosecond photoionization, observed at $\hbar\omega = 50$ eV, disappears in this case.

glie wavelength of the ejected electron-wave packets, and n is the order of the interference peak. To examine the long-range Coulomb effects, we have freely propagated the wave packets to large distances (> 60 bohr) but still find little change in the first interference angle.

To resolve the discrepancy between our calculated diffraction angles and the predictions of the classical formula, we increased the photon energy of the xuv pulses from $\hbar\omega \approx 210$ to 630 eV and performed a series of calculations whose results are listed in Table I. We observe that the discrepancy decreases as the xuv photon energy increases. Above $\hbar\omega \approx 350$ eV, the classical first-order diffraction angle (ϕ_1) is exactly recovered from our TDSE calculations. Two such examples are shown in Figs. 12(a) and 12(b), in which the electron probability densities are plotted for $\hbar\omega \approx 350$ eV and $\hbar\omega \approx 630$ eV, respectively. Interestingly, at

TABLE I. Comparison of the “double-slit” interference angles of the “classical” double-slit (DS) formula and our TDSE calculations, as the photon energy ($\hbar\omega$) varies.

$(\hbar\omega)$ (eV)	λ_e (bohr)	Classical DS angles (ϕ_n) (deg)	TDSE angles (ϕ_n) (deg)
170	1.9587	$\phi_1 \approx 75.3^\circ$	$\phi_1 \approx 52.0^\circ$
210	1.7274	$\phi_1 \approx 58.5^\circ$	$\phi_1 \approx 49.5^\circ$
250	1.5258	$\phi_1 \approx 50.5^\circ$	$\phi_1 \approx 46.5^\circ$
300	1.4104	$\phi_1 \approx 44.1^\circ$	$\phi_1 \approx 42.3^\circ$
350	1.2955	$\phi_1 \approx 39.7^\circ$	$\phi_1 \approx 39.9^\circ$
430	1.1588	$\phi_1 \approx 34.9^\circ$	$\phi_1 \approx 34.8^\circ$
630	0.9462	$\phi_1 \approx 28.0^\circ$ $\phi_2 \approx 69.1^\circ$	$\phi_1 \approx 28.4^\circ$ $\phi_2 \approx 60.7^\circ$

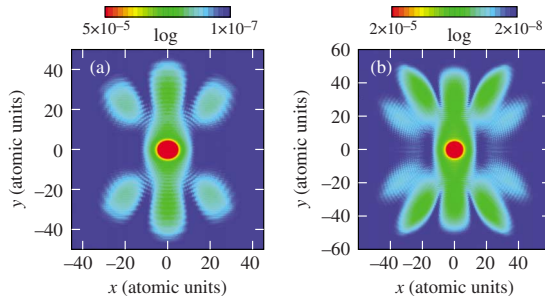


FIG. 12. (Color online) The electron probability densities of H_2^+ at the end of the attosecond xuv pulses at perpendicular polarization, for (a) $\hbar\omega=350$ eV and (b) $\hbar\omega=630$ eV. Different field strengths are applied to obtain noticeable ionization. Classical double-slit interference angles are recovered when $n\lambda_e \leq 65\% R_0$ is satisfied (see more discussions in text).

the highest-photon energy (630 eV), the second-order diffraction patterns appear. The resulting angle (ϕ_2) disagrees, however, with the classical double-slit prediction (see Table I), although ϕ_1 remains in good agreement with the classical formula. These results indicate that the validity of the classical double-slit prediction requires that $n\lambda_e \leq 0.65 R_0$. If the interference path difference ($n\lambda_e$) becomes comparable to the internuclear distance R_0 , the paths are no longer independent and the classical double-slit condition ($\lambda \ll d$ where d , the separation of two slits, is equivalent to R_0 here) is not satisfied. These results could guide the proper choice of photon energy for attosecond photoelectron imaging.

For the parallel case, the wave packets scattered from both nuclei also interfere with each other. However, the interference patterns shown in Figs. 11(a) and 11(b) are much weaker in comparison to the perpendicular case. This may be attributed to the fact that the wave packets scattered from the second nucleus have a time delay relative to those from the first nucleus. While, in the perpendicular case both wave packets scattered from two nuclei always appear simultaneously.

Finally, to have a sense of the energy sharing between the electron and the nuclei during the attosecond ionization, we calculated the nuclear momentum spectrum for the wave packets associated with the ionized electron. The result, presented in Fig. 13 for the parallel polarization cases with two different field strengths $E=0.53$ a.u. and $E=0.053$ a.u. at $\hbar\omega=50$ eV, shows a transfer of less than ~ 0.1 eV of photon energy to the nuclear motion during the attosecond photoionization process. The higher the field, the less the energy transferred to the nuclear motion during the photoionization. Note that the same behavior is also seen in the perpendicular polarization case.

IV. CONCLUSION

In summary, we have investigated the attosecond xuv pulse ionization of H_2^+ by numerically solving the 4D, time-dependent Schrödinger equation. Our results indicate that the single-photon ionization of H_2^+ has a strong orientation dependence at low-photon energies, for which the released

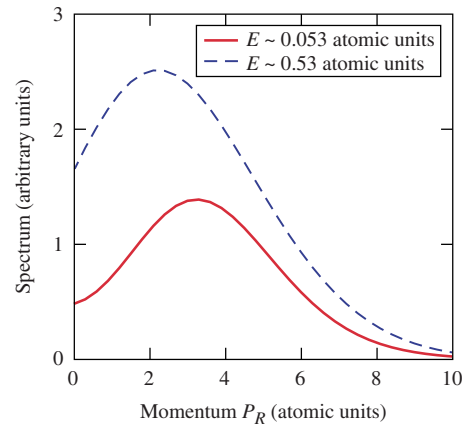


FIG. 13. (Color online) The nuclear momentum spectrum for the parallel polarization cases at $\hbar\omega=50$ eV.

electron has a de Broglie wavelength longer than the internuclear distance. The rescattered electron sees a larger geometrical cross section from the perpendicular direction, which therefore facilitates more ionization. With increasing the photon energy, this photoionization anisotropy disappears due to the fact that the “fast” outgoing electron can distinguish the nuclear scattering centers. As a consequence, single-electron double-slit-like interference patterns emerge in the perpendicular polarization configuration. A series of calculations with higher-photon energies have been performed to explore the classical Young’s double-slit condition. We found that to recover the diffraction angle (ϕ_n) predicted by the classical Young’s double-slit formula, the identified condition of $n\lambda_e \leq \sim 0.65 R_0$ needs to be satisfied. Namely, the electron wavelength must be less than $\sim 65\%$ of the internuclear distance for the first diffraction angle to be the same as the classical double-slit prediction, which guarantees each scattering pathway to be independent. These results provide an important guide for attosecond photoelectron imaging of molecules. While for this study the effects of the nuclear motion remained small, as evidenced by the similar results produced from fixed-nuclei (3D) and 4D calculations, the full capacity of our 4D approach will be explored in the future by examining in greater detail non-Born-Oppenheimer effects in intense field-molecule interactions.

ACKNOWLEDGMENT

This work was supported by the U.S. Department of Energy, Office of Inertial Confinement Fusion under Cooperative Agreement No. DE-FC52-08NA28302, the University of Rochester, and the New York State Energy Research and Development Authority. S.X.H is grateful for the support from the Laboratory for Laser Energetics at the University of Rochester. The Los Alamos National Laboratory (LANL) is operated by Los Alamos National Security, LLC for the National Nuclear Security Administration of the U.S. Department of Energy under Contract No. DE-AC52-06NA25396. Calculations performed under Institutional Computing at LANL on the Coyote and Lobo platforms.

- [1] F. Krausz and M. Ivanov, *Rev. Mod. Phys.* **81**, 163 (2009).
- [2] M. Nisoli and G. Sansone, *Prog. Quantum Electron.* **33**, 17 (2009).
- [3] P. Agostini and L. F. Dimauuro, *Rep. Prog. Phys.* **67**, 813 (2004).
- [4] Y. I. Salamin, S. X. Hu, K. Z. Hatsagortsyan, and C. H. Keitel, *Phys. Rep.* **427**, 41 (2006).
- [5] M. Drescher, M. Hentschel, R. Kienberger, M. Uiberacker, V. Yakovlev, A. Scrinzi, T. Westerwalbesloh, U. Kleineberg, U. Heinzmann, and F. Krausz, *Nature (London)* **419**, 803 (2002).
- [6] M. Uiberacker, T. Uphues, M. Schultze, A. J. Verhoef, V. Yakovlev, M. F. Kling, J. Rauschenberger, N. M. Kabachnik, H. Schröder, M. Lezius, K. Kompa, H.-G. Müller, M. J. J. Vrakking, S. Hendel, U. Kleineberg, U. Heinzmann, M. Drescher, and F. Krausz, *Nature (London)* **446**, 627 (2007).
- [7] S. X. Hu and L. A. Collins, *Phys. Rev. Lett.* **96**, 073004 (2006); *J. Mod. Opt.* **54**, 943 (2007).
- [8] S. Gräfe, V. Engel, and M. Yu. Ivanov, *Phys. Rev. Lett.* **101**, 103001 (2008).
- [9] X. M. Tong and C. D. Lin, *Phys. Rev. A* **73**, 042716 (2006).
- [10] T. Remetter, P. Johnsson, J. Mauritsson, K. Varjú, Y. Ni, F. Lépine, E. Gustafsson, M. F. Kling, J. Khan, R. López-Martens, K. J. Schafer, M. J. J. Mrakking, and A. L'Huillier, *Nat. Phys.* **2**, 323 (2006).
- [11] K. J. Schafer, M. B. Gaarde, A. Heinrich, J. Biegert, and U. Keller, *Phys. Rev. Lett.* **92**, 023003 (2004).
- [12] A. D. Bandrauk, S. Chelkowski, D. J. Diestler, J. Manz, and K.-J. Yuan, *Phys. Rev. A* **79**, 023403 (2009), and references therein.
- [13] S. X. Hu, J. Colgan, and L. A. Collins, *J. Phys. B* **38**, L35 (2005).
- [14] J. S. Parker, B. J. S. Doherty, K. T. Taylor, K. D. Schultz, C. I. Blaga, and L. F. DiMauro, *Phys. Rev. Lett.* **96**, 133001 (2006).
- [15] X. Guan, K. Bartschat, and B. I. Schneider, *Phys. Rev. A* **77**, 043421 (2008); X. Guan, O. Zatsarinny, K. Bartschat, B. I. Schneider, J. Feist, and C. J. Noble, *ibid.* **76**, 053411 (2007); J. Feist, S. Nagele, R. Pazourek, E. Persson, B. I. Schneider, L. A. Collins, and J. Burgdörfer, *ibid.* **77**, 043420 (2008).
- [16] S. X. Hu and L. A. Collins, *Phys. Rev. A* **73**, 023405 (2006); *J. Phys. B* **39**, L185 (2006).
- [17] L. B. Madsen and M. Plummer, *J. Phys. B* **31**, 87 (1998); S. X. Hu, W. X. Qu, and Z. Z. Xu, *Phys. Rev. A* **57**, 3770 (1998); T. K. Kjeldsen and L. B. Madsen, *Phys. Rev. Lett.* **95**, 073004 (2005); C. B. Madsen and L. B. Madsen, *Phys. Rev. A* **74**, 023403 (2006).
- [18] A. D. Bandrauk, S. Chelkowski, S. Kawai, and H. Lu, *Phys. Rev. Lett.* **101**, 153901 (2008).
- [19] M. Magrakvelidze, F. He, S. De, I. Bocharova, D. Ray, U. Thumm, and I. V. Litvinyuk, *Phys. Rev. A* **79**, 033408 (2009).
- [20] W. X. Qu, S. X. Hu, and Z. Z. Xu, *Phys. Rev. A* **57**, 2219 (1998); **57**, 4528 (1998).
- [21] S. Chelkowski, T. Zuo, O. Atabek, and A. D. Bandrauk, *Phys. Rev. A* **52**, 2977 (1995).
- [22] V. Roudnev, B. D. Esry, and I. Ben-Itzhak, *Phys. Rev. Lett.* **93**, 163601 (2004).
- [23] F. He, C. Ruiz, and A. Becker, *Phys. Rev. Lett.* **99**, 083002 (2007); F. He, A. Becker, and U. Thumm, *ibid.* **101**, 213002 (2008).
- [24] M. Førre and H. Bachau, *Phys. Rev. A* **77**, 053415 (2008).
- [25] B. I. Schneider and L. A. Collins, *J. Non-Cryst. Solids* **351**, 1551 (2005).
- [26] B. I. Schneider, L. A. Collins, and S. X. Hu, *Phys. Rev. E* **73**, 036708 (2006).
- [27] J. R. Hiskes, *Phys. Rev.* **122**, 1207 (1961).
- [28] H. Stapelfeldt and T. Seideman, *Rev. Mod. Phys.* **75**, 543 (2003), and references therein.
- [29] R. Dörner, V. Mergel, O. Jagutzki, L. Spielberger, J. Ullrich, R. Moshhammer, and H. Schmidt-Böcking, *Phys. Rep.* **330**, 95 (2000).
- [30] L. A. Collins, J. D. Kress, and R. B. Walker, *Comput. Phys. Commun.* **114**, 15 (1998).
- [31] S. X. Hu, *Phys. Rev. Lett.* **98**, 133201 (2007); *Phys. Rev. A* **74**, 062716 (2006).
- [32] I. Carusotto, S. X. Hu, L. A. Collins, and A. Smerzi, *Phys. Rev. Lett.* **97**, 260403 (2006); T. P. Simula, N. Nygaard, S. X. Hu, L. A. Collins, B. I. Schneider, and K. Mølmer, *Phys. Rev. A* **77**, 015401 (2008); T. P. Simula, T. Mizushima, and K. Machida, *Phys. Rev. Lett.* **101**, 020402 (2008).
- [33] S. X. Hu and Z. Z. Xu, *Phys. Rev. A* **56**, 3916 (1997); S. X. Hu and Z. Z. Xu, *Appl. Phys. Lett.* **71**, 2605 (1997).
- [34] H. Wind, *J. Chem. Phys.* **42**, 2371 (1965). The ground state minimum occurs at $R_0=2.0$ a.u. at an energy of -0.60263 hartrees, and the zero-point vibrational energy is about 0.0102 a.u.
- [35] A. Staudte, S. Patchkovskii, D. Pavicic, H. Akagi, O. Smirnova, D. Zeidler, M. Meckel, D. M. Villaeneuve, R. Dörner, M. Y. Ivanov, and P. B. Corkum, *Phys. Rev. Lett.* **102**, 033004 (2009).
- [36] H. D. Cohen and U. Fano, *Phys. Rev.* **150**, 30 (1966).
- [37] M. Walter and J. Briggs, *J. Phys. B* **32**, 2487 (1999).
- [38] J. Fernández, O. Fojón, A. Palacios, and F. Martín, *Phys. Rev. Lett.* **98**, 043005 (2007).
- [39] D. A. Horner, S. Miyabe, T. N. Rescigno, C. W. McCurdy, F. Morales, and F. Martín, *Phys. Rev. Lett.* **101**, 183002 (2008).
- [40] D. Rolles, M. Braune, S. Cvejanovic, O. Geßner, R. Hentges, S. Korica, B. Langer, T. Lischke, G. Prümper, A. Reinköster, J. Viehhaus, B. Zimmermann, V. McKoy, and U. Becker, *Nature (London)* **437**, 711 (2005).